Article

Far-Field Maximal Power Absorption of a Bulging Cylindrical Wave Energy Converter

Matthieu Ancellin [1,2], Marlène Dong [1], Philippe Jean [3] and Frédéric Dias [1,2,]*

[1] UCD School of Mathematics and Statistics, University College Dublin, D04 V1W8 Dublin, Ireland; matthieu.ancellin@ens-paris-saclay.fr (M.A.); marlene.dong@polytechnique.edu (M.D.)
[2] ENS Paris-Saclay, CNRS, Centre Borelli, Université Paris-Saclay, 91190 Gif-sur-Yvette, France
[3] SBM Offshore, 24 Avenue de Fontvieille, 98007 Monaco City, Monaco; philippe.jean@sbmoffshore.com
[*] Correspondence: frederic.dias@ucd.ie

check for updates

Abstract: The maximal power that is absorbed by a wave energy converter can be estimated from the far-field behavior of the waves that are radiated by the device. For realistic estimates, constraints must be used to enforce restrictions on the set of admissible motions when deriving the maximal absorption width. This work is dedicated to the numerical computation of the maximal absorption width under constraints for devices with several non-trivial degrees of freedom. In particular, the method is applied to a model of SBM Offshore's S3 wave energy converter, a bulging horizontal cylinder. The results are compared with a more classical approach, which consists of computing the linear dynamic response of the wave energy converter interacting with the waves. The far-field maximal absorption width can be seen as an upper bound to evaluate what would be the power captured by a perfect control strategy. The method also shows that the absorption width of the S3 wave energy converter is larger for wavelengths that are smaller than the device length. In practice, this means that S3 wave energy converters will be longer than the maximal wavelength to be captured on the targeted production site.

Keywords: marine renewable energy; wave energy; fluid-structure interaction

1. Introduction

In recent years, flexible wave energy converters (WECs) have appeared to be a promising direction for overcoming some of the limitations of rigid WECs. Several studies have presented theoretical and numerical models of flexible WECs. Desmars et al. [1] modeled the power take-off of a submerged flexible horizontal "wave carpet". Tay and Wei [2] discussed the role of the flexibility in the efficiency of a pontoon-type WEC. Mei [3] studied the non-linear behavior of a submerged open horizontal cylinder device called "Anaconda". Renzi [4] investigated the hydroelectromechanical-coupled dynamics of a piezoelectric wave energy converter. The converter was made of a flexible bimorph plate, clamped at its ends, and forced to motion by incident ocean surface waves. In the present paper, we are interested in a device that was designed by SBM Offshore, namely the S3 device, which is a submerged closed horizontal cylinder that has been previously studied by Babarit et al. [5].

During the design phase of a wave energy converter (WEC), several analytical and numerical methods are available to estimate the power absorbable by the device. In the early stages of the design, the most popular model is linear potential flow theory combined with a Boundary Element Method (BEM) solver [6,7]. Often, the result of the BEM solver is used in order to evaluate the interaction forces between the floating body and the fluid, and to predict the dynamics of the body. Unlike simpler rigid bodies (e.g., rigid floating buoys with at most six degrees of freedom (dof)), flexible systems with many

dofs may require a long custom modeling effort to simulate their dynamics. Subsequently, it might be useful to have a coarse model that allows one to quickly evaluate the efficiency of a given design.

In the present paper, we are interested in a coarser model that does not require the modeling of the inner dynamics of the device. It relates the far-field waves radiated by the device to the maximal absorption width. It has been presented and applied in several papers, such as [7–10]. Because it only requires the resolution of a few linear potential flow radiation problems, it is one of the simplest methods available to evaluate the power that is absorbable by the device. By absorbable power, we mean transmissible from the waves to a motion or deformation of the WEC, disregarding the subsequent conversion of the energy, which is not modeled. The problem is only a fluid-structure interaction problem and the power take-off system is not discussed in this paper.

The goal of the present work is to test and validate the approach based on far-field radiated waves on an actual industrial device. To this end, a lightweight numerical tool has been developed, allowing for quickly evaluating the efficiency of any device with several dofs, including non-trivial deformation dofs. To our knowledge, no previous work considered this far-field method in such a general framework.

A preliminary version of this work has appeared in [11]. The present paper includes a more precise model of the physics of the cylinder and some comparisons with the more traditional linear response model, based on [12]. Additionally, the amplitude of the incoming waves was ignored in [11,12], but is now discussed in the present paper.

In Sections 2.1 and 2.2, the far-field method for the estimation of the absorption width is presented. In Section 2.3, the SBM Offshore's S3 WEC and its modeling are introduced. In particular, the analysis of the deformation modes conducted by Babarit et al. [5] is summarized. Numerical results are presented and discussed in Section 3.

2. Theory

2.1. Far-Field Maximal Absorption Width without Constraint

Let us consider a linear potential flow in the frequency domain. Here, we follow the conventions of [7] and we refer to that book for more details on the derivation of the following formulas. Note that Newman in [8] uses a different convention for the definition of the Kochin functions: $H_{\text{Newman}} = 4\pi k\, H$, where k is the wavenumber. The convention for time dependence is also different: $x(t) = \Re\left(\hat{x}_{\text{Newman}}e^{i\omega t}\right)$ whereas it is $x(t) = \Re\left(\hat{x}e^{-i\omega t}\right)$ in this paper, where $\Re$ is the real part. For the sake of simplicity, all of the computations in this paper are performed assuming an infinite water depth, although similar formulas exist in the finite depth case.

In the far field, the radiated wave can be described by the complex-valued Kochin function $H(\theta)$, where θ is a direction of interest. It can be related to the complex-valued velocity potential Φ in cylindrical coordinates (R, θ, z) as

$$\Phi(R, \theta, z) = 4\pi\sqrt{\frac{1}{\lambda R}}H(\theta)f_0(z)e^{i\left(2\pi\frac{R}{\lambda} + \frac{\pi}{4}\right)} + O\left(\frac{1}{R^{3/2}}\right),\tag{1}$$

where f_0 is a function of the vertical coordinate z only and λ is the wavelength of the waves.

Because we consider a linear problem, the potential of the radiated waves and the associated Kochin function can be decomposed as a sum of contributions from each dof taken independently. In the frequency domain, a body motion is defined by n_{dof} complex values $\hat{a}_j$ that represent the amplitude of the dof j. We can then write $H = \sum_j^{n_{\text{dof}}} \hat{a}_j H_j$, where H_j is the Kochin function for a unit excitation of the dof j.

We use the absorption width W to measure the efficiency of the WEC. It is the ratio between the mean absorbed power (in watts) and mean power flux of the incoming waves (in watts per meter). Thus, it has the dimension of a length.

By writing an energy balance around a WEC (Equation (4.21) of [7]), we can derive an expression for the absorption width W. Assuming incoming waves with a complex-valued amplitude $\hat{A}$ and a WEC oscillating with complex-valued dof amplitudes $\hat{a} = (\hat{a}_1, \ldots, \hat{a}_{n_{\text{dof}}}) \in \mathbb{C}^{n_{\text{dof}}}$, we have:

$$W(\hat{a}, \hat{A}, k, \beta) = 8\pi k \Im \left(\sum_{j=1}^{n_{\text{dof}}} \frac{\hat{a}_j}{\hat{A}} H_j^*(k, \pi + \beta) \right) - 8\pi k^3 \int_0^{2\pi} \left| \sum_{j=1}^{n_{\text{dof}}} \frac{\hat{a}_j}{\hat{A}} H_j(k, \theta) \right|^2 d\theta,$$

(2)

where $\Im$ is the imaginary part, the star denotes the complex conjugate, k is the wavenumber, and β is the direction of the incoming waves (in radian).

The first term of (2) depends on the Kochin function downstream of the WEC as well as the phase of $\hat{a}_j / \hat{A}$, which is the difference of phase between the motion of the dof j and the incoming waves. The second term of (2) is the total amount of energy lost by radiation by the WEC in all directions and is independent of this difference of phase.

Diffraction does not explicitly appear in (2). Physically, it can be understood by the fact that no energy can be absorbed by a fixed non-radiating body. Mathematically, we refer to Equation (4.20) of [7].

The above expression can be reformulated in the following way. Let us consider a floating body in free motion in a wave field. Part of the incoming energy is dissipated or captured by the device, while the rest escapes in the diffracted and radiated fields. Let us now force the exact same motion to the same WEC in a still ocean without incoming waves. The pattern of the waves radiated by the forced body is sufficient to compute the power that was dissipated or absorbed in the free motion experiment. Analyzing all of the wave patterns that can be radiated by a body with a given shape gives us a clue on the maximal power that could be absorbed by a body with such a geometry.

The above expression relates a given motion of the WEC to the power absorbable by this motion for a given wave field $(\hat{A}, k, \beta)$. The maximal absorbable power can be found as the maximum over all possible motions of the body. The maximal absorption width reads

$$W^{\text{optimal}}(\hat{A}, k, \beta) = \max_{\hat{a} \in \mathbb{C}^{n_{\text{dof}}}} \left[W(\hat{a}, \hat{A}, k, \beta) \right].$$

(3)

The absorption width only depends on $\hat{a} / \hat{A}$, so the solution for all $\hat{A}$ can be deduced from the resolution of the problem for a single value of $\hat{A}$.

Besides, this optimization problem can be slightly simplified thanks to the following remark: for a given motion of the WEC, the first term of (2) varies with the difference of phase between $\hat{a}$ and $\hat{A}$ as a sine function between $-8\pi k \left| \sum_j \frac{\hat{a}_j}{\hat{A}} H_j^* \right|$ and $8\pi k \left| \sum_j \frac{\hat{a}_j}{\hat{A}} H_j^* \right|$. When we are looking for the best absorption width, the difference of phase can be assumed to be optimal and the first term maximal. We will denote this situation as the WEC being *in phase* with the incoming waves.

Using this fact, we can rewrite (3), as

$$W^{\text{optimal}}(\hat{A}, k, \beta) = \max_{\hat{a} \in \mathbb{R} \times \mathbb{C}^{n_{\text{dof}}-1}} \left[W^{\text{in phase}}(\hat{a}, \hat{A}, k, \beta) \right],$$

(4)

where $W^{\text{in phase}}$ is defined as

$$W^{\text{in phase}}(\hat{a}, \hat{A}, k, \beta) = 8\pi k \left| \sum_{j=1}^{n_{\text{dof}}} \frac{\hat{a}_j}{\hat{A}} H_j^*(k, \pi + \beta) \right| - 8\pi k^3 \int_0^{2\pi} \left| \sum_{j=1}^{n_{\text{dof}}} \frac{\hat{a}_j}{\hat{A}} H_j(k, \theta) \right|^2 d\theta.$$

(5)

This analytical optimization of the difference of phase between the WEC and the incoming waves reduces the dimension of the space of candidate motions from $2n_{\text{dof}}$ to $2n_{\text{dof}} - 1$.

For a single dof ($n_{\mathrm{dof}} = 1$), the absorption width W is a quadratic function of $|\hat{a}|$, where $\hat{a}$ is the complex-valued amplitude of the dof. This function has a maximum $|\hat{a}|^{\mathrm{optimal}}$, which reads (also see [8])

$$|\hat{a}|^{\mathrm{optimal}}(\hat{A}, k, \beta) = \frac{|\hat{A}|}{2k^2} \frac{|H(k, \pi + \beta)|}{\int_0^{2\pi} |H(k, \theta)|^2 d\theta}, \qquad W^{\mathrm{optimal}}(\hat{A}, k, \beta) = \frac{2\pi}{k} \frac{|H(k, \pi + \beta)|^2}{\int_0^{2\pi} |H(k, \theta)|^2 d\theta}. \qquad (6)$$

Using the assumption of a slender body, Newman [8] and Farley [9] have derived analytical expressions for the maximal absorption width for a deformation along a single dof.

A generalization of (6) for several dofs can be found in Equation (4.24) of [7]. It takes the form of a complex-valued linear system of n_{dof} equations, since the function to maximize has the form of a quadratic function of $\hat{a}$.

Another relation can be useful for studying the maximal absorption width of a WEC [13]:

$$\frac{k}{2\pi} \int_0^{2\pi} W^{\mathrm{optimal}}(\hat{A}, k, \beta) \, d\beta = n_{\mathrm{dof}}, \qquad (7)$$

where n_{dof} is the number of hydrodynamically independent dofs (that will not be distinguished from the total number of dofs in this paper). For a single dof, (7) can be easily derived from (6). On average over all incoming wave directions, all of the bodies and dofs have the same maximal absorption width. In [11], this fact has been illustrated on the example of a simple rigid body moving in heave or in surge. The W^{optimal} of the heaving body is independent of the direction of the incoming waves, whereas the W^{optimal} of the surging body varies as $\cos(\beta)$. It is maximal when the direction of motion and the incoming waves are aligned and zero when they are orthogonal. However, one can check that, on average, over all wave directions, both maximal absorption widths are the same and are independent of the shape of the body.

2.2. Far-Field Maximal Absorption Width under Constraint

If the absorbable power of a WEC was indeed independent of the body shape and of its dofs, as suggested by (7), all research on wave energy would be simpler. Unfortunately, the reasoning above has several shortcomings. The main one is the following: the amplitude $|\hat{a}|^{\mathrm{optimal}}$ at which the absorbed power would be maximal is often not reachable by the devices. The amplitude is constrained by, for instance, mooring for translation motion or elastic properties of the material for a deformable WEC. The range on which the electric system can extract energy can also constrain the "useful" amplitude of the dof.

For a single dof, the constraint can easily be taken into account in the analytical expression (6) (see also [8]):

$$|\hat{a}|^{\mathrm{optimal}}(\hat{A}, k, \beta, b) = \min\left(\frac{|\hat{A}|}{2k^2} \frac{|H(\pi + \beta)|}{\int_0^{2\pi} |H(\theta)|^2 d\theta}, b \right),$$
$$W^{\mathrm{optimal}}(\hat{A}, k, \beta, b) = W^{\mathrm{in\ phase}}(|\hat{a}|^{\mathrm{optimal}}, \hat{A}, k, \beta), \qquad (8)$$

where $b \in \mathbb{R}^+$ is the maximal admissible amplitude.

For several dofs, an optimization under constraint problem has to be solved:

$$W^{\mathrm{optimal}}(\hat{A}, k, \beta, \mathcal{D}) = \max_{\hat{a} \in \mathcal{D}} \left[W^{\mathrm{in\ phase}}(\hat{a}, \hat{A}, k, \beta) \right], \qquad (9)$$

where $\mathcal{D} \subset \mathbb{R} \times \mathbb{C}^{n_\mathrm{dof}-1}$ is the set of admissible motions of the WEC. In this work, the constraint takes the form of a l_2-norm on the vector of complex-valued amplitudes $\hat{a}$, which is

$$\mathcal{D} = \left\{ \hat{a} \in \mathbb{R} \times \mathbb{C}^{n_\mathrm{dof}-1} \,\middle|\, \sum_{i=1}^{n_\mathrm{dof}} |\hat{a}_i|^2 \leq b^2 \right\} \tag{10}$$

for a given $b \in \mathbb{R}^+$.

In general, the l_2-norm of $\hat{a}$ does not have a physical interpretation and this type of constraint has only been chosen for its simplicity of implementation in an optimization software. It might be possible to derive an analytical expression for the maximal absorption width under constraint, as in the one-dimensional (1D) case, at least for such a simple constraint. This has not be done in this work, where we used an optimization algorithm to find the optimum.

Without the constraint, the problem is linear, in the sense that it only depends on $\hat{a}/\hat{A}$. With a constraint, such as (10), this is not the case anymore: the amplitude of the incoming waves and the amplitude of the body motion are independent. In the rest of the paper, we will keep working with the normalized amplitude $\hat{a}/\hat{A}$ and apply the constraint in the following form:

$$\sum_i |\hat{a}_i|^2 \leq b^2 \qquad \Longleftrightarrow \qquad \sum_i \left|\frac{\hat{a}_i}{\hat{A}}\right|^2 \leq \frac{b^2}{|\hat{A}|^2}. \tag{11}$$

The constraint on the right-hand side of Equation (11) means that the change of the amplitude of the incoming wave is equivalent to a change in the constraint b. Indeed, when the amplitude of the waves is small, the system will be able to capture the incoming energy without breaking the constraint and the problem can be seen as unconstrained. On the other hand, cases with high wave amplitude will be more affected by the constraint of the body motion.

2.3. Modal Analysis of the SBM Offshore's S3 Device

The S3 device consists of a water-filled horizontal elastic tube floating just beneath the sea surface. When ocean waves travel above it, they apply a time-varying pressure on the tube wall that induces local changes in diameter. This creates bulge waves in the tube. Subsequently, the elastic deformation is converted into electricity thanks to its electroactive attribute.

We model the device as a horizontal cylinder, parallel to the free surface, with z_S the depth of its axis. Let L be the length of the cylinder (constant) and S_S its cross section at rest (that is when the device is immersed but static). The cylinder is modeled as a one-dimensional (1D) system (since $L \gg \sqrt{S_S}$) and its deformation is assumed to be axisymmetric. We denote, by $S(x,t)$, the cross section at position $x \in [-L/2, L/2]$ and at time t (see Figure 1 for a schematic of the system).
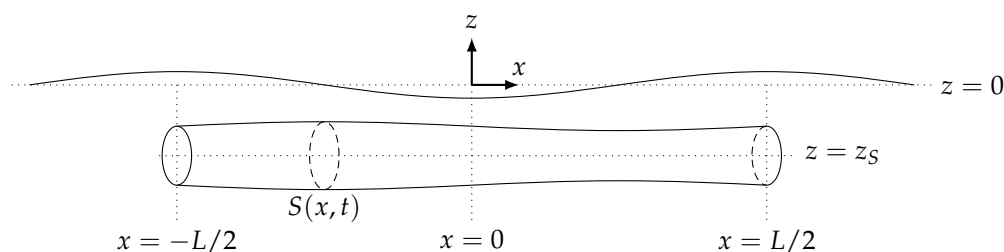

Figure 1. Schematic of a bulging S3 wave energy converter, as studied in the paper.

Following Babarit et al. [5], we define $\chi(x,t)$, such that $\partial \chi / \partial t = U(x,t)$, where U is the velocity of the fluid inside the cylinder. From mass conservation, one has

$$s(x,t) = S(x,t) - S_S = -S_S \frac{\partial \chi}{\partial x}. \tag{12}$$

Because we are studying the linear regime of small deformations, the radial motion of a point on the surface of the cylinder can be computed as

$$r(x,t) - r_S = r_S \left(\sqrt{1 - \frac{\partial \chi}{\partial x}} - 1 \right) \simeq -\frac{r_S}{2} \frac{\partial \chi}{\partial x}, \tag{13}$$

where r_S is the radius at rest.

Neglecting the damping and the interaction with the outer fluid, the following wave equation can be derived:

$$\frac{\partial^2 \chi}{\partial t^2} - \frac{1}{\rho D} \frac{\partial^2 \chi}{\partial x^2} + \frac{T_s}{4\pi\rho} \frac{\partial^4 \chi}{\partial x^4} = 0, \tag{14}$$

where D is the distensibility of the membrane, T_S the tension in the wall of the tube at rest, and ρ the density of the fluid. We look for a solution of the form $\chi(x,t) = \Re(\hat{\chi}(x)e^{-i\omega t})$. The resolution is thoroughly developed in Appendix B of [5]. Modes of deformations $\chi_n(x)$ are expressed for each frequency ω_n and wavenumber k_n satisfying the dispersion relation derived from (14). The modes are normalized while using the scalar product

$$\langle \chi_i, \chi_j \rangle = \frac{1}{L} \int_{-L/2}^{L/2} \chi_i \chi_j dx + \frac{M}{\rho S_S L} \left. \chi_i \right|_{L/2} \left. \chi_j \right|_{L/2}. \tag{15}$$

Figure 2 shows the first five modes of the WEC that we consider. The parameters used for the model can be found in Table 1.
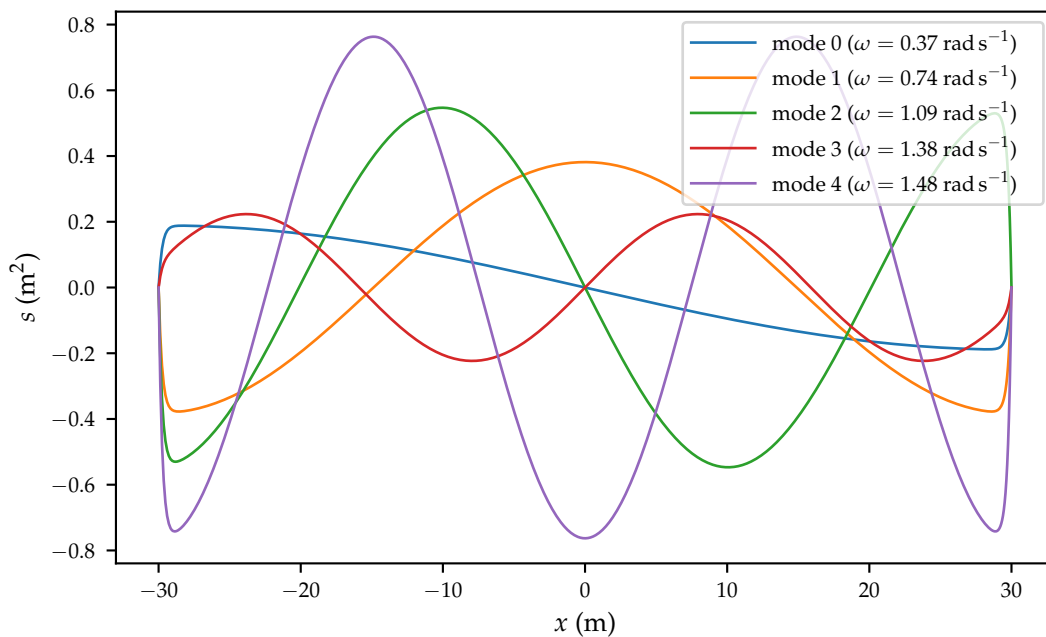

Figure 2. Deformation of the first five modes plotted in terms of the cross section s introduced in Equation (12) for the parameters given in Table 1. The modes are normalized using the scalar product (15).

Table 1. Parameters used for the model of the WEC.

length L	$60\,\mathrm{m}$
radius r_S	$0.9\,\mathrm{m}$
cross section S_s	$2.544\,\mathrm{m}^2$
z_S	$-1.35\,\mathrm{m}$
D	$2.248 \times 10^{-5}\,\mathrm{Pa}^{-1}$
T_s	$3.8 \times 10^4\,\mathrm{N}$
M	$38{,}000\,\mathrm{kg}$
η	$0.323\,\mathrm{m}^2\,\mathrm{s}^{-1}$
B_R	$8\pi \cdot 10^{-6}$
water density ρ	$1025\,\mathrm{kg}\,\mathrm{m}^{-3}$

By introducing into the full equation of motion of the WEC

$$\chi(x,t) = \sum_{i=1}^{n_{\mathrm{dof}}} a_i(t)\chi_i(x) = \Re\left(\sum_{i=1}^{n_{\mathrm{dof}}} \hat{a}_i \chi_i(x) e^{-i\omega t} \right), \tag{16}$$

where χ_i is the normalized i-th mode, one obtains the following discrete equation of motion on the coefficients $\hat{a} = (\hat{a}_i)_i$, where $\hat{a}_i$ is the complex-valued amplitude of the dof i in the frequency domain:

$$\left(-\omega^2(\rho S_s L + A(\omega)) + i\omega(B(\omega) + \rho S_s \eta \xi + \rho B_R \epsilon) + \rho S_s L \omega_{\mathrm{dof}}^2 \right) \hat{a} = F_{ex}(\omega). \tag{17}$$

Here, A is the added mass matrix, B is the radiation damping matrix, η is the dissipation coefficient, ξ is the wall damping matrix

$$\xi_{ij} = \int_{-L/2}^{L/2} \frac{\partial \chi_i}{\partial x} \frac{\partial \chi_j}{\partial x} \mathrm{d}x,$$

B_R is a damping parameter that is related to viscosity, ϵ is the inner flow damping matrix

$$\epsilon_{ij} = \int_{-L/2}^{L/2} \chi_i \chi_j \mathrm{d}x,$$

ω_{dof} is the diagonal matrix of the pulsations of the modes of the cylinder, and F_{ex} is the excitation force. The mean power dissipated by the material can be computed as

$$P(\omega) = \frac{1}{2}\rho S_s \eta \omega^2 \sum_m \sum_l \Re(\hat{a}_m \hat{a}_l^*) \xi_{ml}. \tag{18}$$

Alternatively, for a given deformation χ, the dissipated power can be evaluated with the help of the far-field Equation (2). One can check that both expressions of the power give the same results [12]. A similar comparison is done in [1,14].

In the previous section, we discussed the definition of a constraint on the amplitude of motion or deformation of a body. It will take the form (11) for the coefficients $\hat{a}$ that are defined in this section. From (12) and (16), we have

$$s(x,t) = \sum_i^{n_{\mathrm{dof}}} a_i(t)s_i(x) = \Re\left(\sum_i^{n_{\mathrm{dof}}} \hat{a}_i s_i(x) e^{-i\omega t} \right), \tag{19}$$

where s_i is the deformation profile of mode i, as plotted for instance on Figure 2. Thus, a constraint on the norm of $\hat{a}$ can be interpreted as a constraint on the minimal and maximal variations of the cross section s. However, the exact relationship between $\max_{x,t} s(x,t)$ and the norm of $\hat{a}$ is unknown. (In particular, the normalization using the scalar product (15) of the modes leads to non-trivial values

of $\max_x |s_i(x)|$ for all i.) For a given bound b in (11), the actual maximal geometrical deformation of the WEC is only checked a posteriori. This is a limitation of the current implementation.

3. Numerical Results

3.1. Implementation and Setup

In [8], an analytical model has been used to compute the radiated wave field of an elongated body by making the approximation of a slender body. Instead, here we have chosen to base our work on full 3D linear potential flow simulations using the open source boundary element method solver Capytaine [15], which is a refactored version of Nemoh [16]. This approach allows for directly using this method on a larger variety of body shapes. For the S3, the modes are computed using the relations given in [5] and the inputs of the BEM solver are the deformations given by (13). The outputs of interest of the BEM solver are the Kochin functions.

The unconstrained optimization problem (3) is solved while using the analytical solution given by [7]. For the constrained optimization problem (9), off-the-shelf optimization algorithms from Scipy [17] have been used, in particular the SLSQP (Sequential Least Squares Quadratic Programming) algorithm, as implemented in [18]. The software is implemented in Python using tools from the Python scientific ecosystem [17,19–21]. The optimizations for several wave frequencies or several incoming wave directions are "embarrassingly parallel" problems and they can straightforwardly be run in parallel.

Because we want to maximize a quadratic function within a convex domain, no convergence difficulty is expected for the optimization algorithm, as long as the constraint is smooth enough. In cases with a low number of dofs, the solution of the optimization algorithm has been validated by comparing with a brute force research of the optimum. The result of the optimization algorithm has also been compared to the analytical solution (Equation (4.24) of [7]) when no constraint is set. See [11] for an example of validation on a simple 2-dof rigid body.

The parameters used for the numerical examples are inspired from a model of a SBM Offshore's S3 of length $L = 60$ m and radius when immersed $r_S = 0.9$ m. All of the parameters are given in Table 1. The wavelengths of interest at sea range from 30 to 200 meters, which is from $0.5L$ to $3L$. The hypothesis of an infinite water depth is made.

3.2. Mesh Convergence Study

A convergence study has been done to quantify the margin of error due to the discretization of the cylinder for the BEM solver. For the same physical parameters, the maximal absorption width has been computed with several discretizations of the cylinder between $N = 60$ and $N = 11850$ panels. As no analytical solution was available, the reference solution has been chosen as the solution with the finer mesh. The relative error for a mesh of N panels has been computed, as follows:

$$e(N) = \frac{|W(N) - W(11850)|}{|W(11850)|}. \tag{20}$$

The reference solution of 11,850 panels requires several gigabytes of Random Access Memory (RAM) to store the matrices of the BEM solver. The memory that is available on a typical laptop or desktop as of 2020 is insufficient for much finer resolution. Numerical techniques allowing to reduce the memory footprint of the solver exist, such as the one discussed in [22] for horizontal cylinders. They have not been used in the present study, but could allow for higher resolution solutions to become the reference in the future.

On Figure 3, the relative error has been plotted for several meshes, several wavelengths, two types of constraints on the maximal deformation and two numbers of modes in the model. For the maximal absorption width without constraint with few modes (top left figure), the error seems to follow a first

order convergence rate: multiplying by 10 the number of cells leads to a division by 10 of the error. It is expected since we use a first order BEM solver.
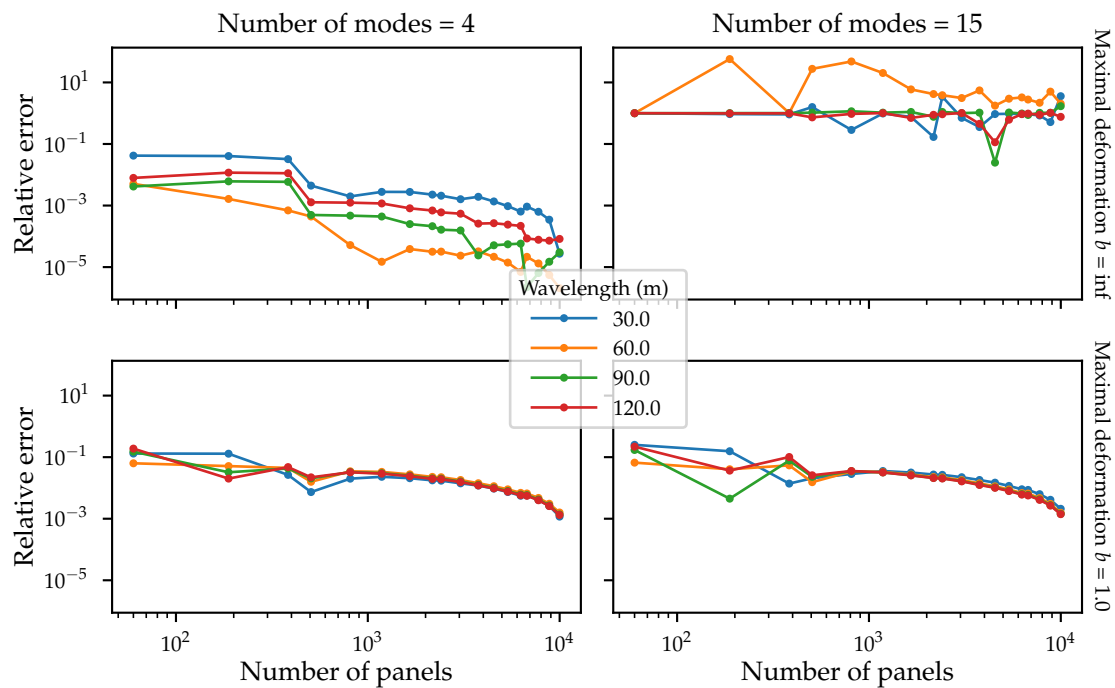

Figure 3. The relative error on the maximal absorption width computed with the first four modes and the first fifteen modes of the S3 with respect to a reference solution with 11850 panels, for several wavelengths and with and without constraint on the maximal deformation ($b \rightarrow \infty$ means no constraint). Table 1 gives the parameters of the problem.

For the maximal absorption width under constraint (bottom left figure), the convergence rate seems to be lower. The relative error is higher for the case under constraint than without constraint, but the absolute value is much lower (as seen in Section 3.4), so the absolute error is actually lower.

When the number of modes is increased, stability problems are observed for the optimization without constraint. At fifteen modes, the results are dominated by noise and no convergence is observed (top right figure). The problem of the optimization without constraint might be too stiff. Further investigation is needed in order to understand this behavior. The maximal deformation can reach absurdly high values (e.g., $\sqrt{\sum |\hat{a}_i|^2} > 10^{15}$), so this case would have been of low practical interest anyway. On the other hand, the maximal deformation with constraint (bottom right figure) does not seem to suffer from the same problem and the same relative error is observed for any number of modes.

In Sections 3.3 and 3.4, the goal is to compare the maximal absorption width with and without constraint. For that purpose, the number of modes is limited. In Section 3.5, the objective is to compare with the linear response of the WEC and have some practical estimation of the efficiency of the device. Thus, the number of modes is increased to fifteen and the unconstrained maximal absorption is not discussed.

As a trade-off between computation time and numerical accuracy, a mesh of 3708 cells is used in the rest of this paper. The relative error due to the size of the mesh is expected to be of a few percents.

Another source of numerical inaccuracy is the approximation of the integral with respect to θ in (2). It has been done with a trapezoid method with 200 points and the relative error due to this discretization is also of 1%.

3.3. Examples of Deformation Profiles

Let us discuss the effect of the constraint on the solution of the optimization problem. On Figure 4, examples of maximal deformation profiles have been plotted for several parameters.
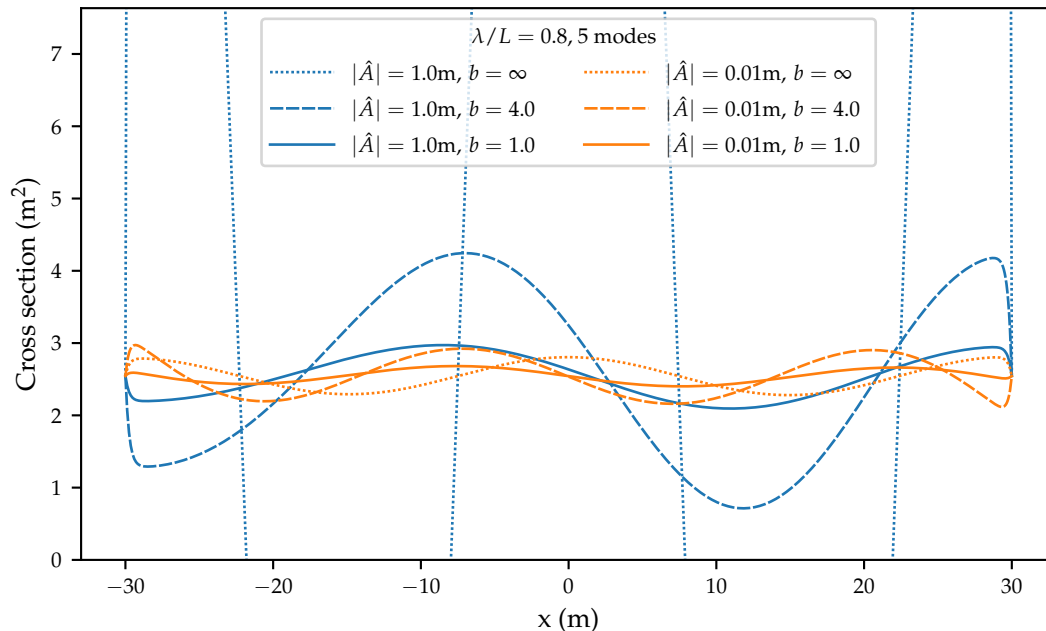

Figure 4. Cross section at a given time of a cylinder with length $L = 60$ m and radius $r_S = 0.9$ m following its maximal motion predicted while using the first five modes of deformation for waves of wavelength $\lambda = 0.8\,L$ traveling in the direction of the device, for several incoming wave amplitudes $|\hat{A}|$ and several constraints b.

The blue lines correspond to a wave amplitude of 1 m. For unconstrained motion (dotted lines), the maximal deformation has no physical meaning (negative cross-section). When a constraint is applied to the optimization process ($b = 4.0$ or $b = 1.0$), the maximal deformations are more physically reasonable. They are actually on the boundary of the domain of the optimization problem, that is $\sum |\hat{a}_i|^2 = b^2$. For a lower wave amplitude (orange line), the deformations are physically meaningful with or without constraint, as discussed above.

Note that the unconstrained deformation profiles for both wave amplitudes (dotted orange line and dotted blue line) are identical up to a scaling of factor 100. This is expected from the linearity of the problem without constraint. For constrained problems, there is no obvious relationship between the deformation profiles at both wave amplitudes.

In the rest of this paper, the maximal absorption width under constraint always corresponds to a constraint of $b = 1.0$, as this order of magnitude appears to give deformations that are reasonably reachable by the device.

3.4. Maximal Absorption Width with and without Constraint

In this section, the maximal absorption width W computed while using the theory of Sections 2.1 and 2.2 is plotted. The results are presented in dimensionless form. Two different dimensionless forms of W are of interest. On one hand, the normalization by the wavenumber k is interesting to retrieve the theoretical result of (7). On the other hand, the normalization by the dimension of the cylinder makes sense from an engineering point of view if the absorption width is geometrically interpreted as the length of wave front that is absorbed by the device. The former is used in this section, whereas the latter is used in the next section.

On Figure 5, the maximal absorption width has been computed for each of the first five eigenmodes of the cylinder individually (that is for five cylinders deforming each one along only one dof).
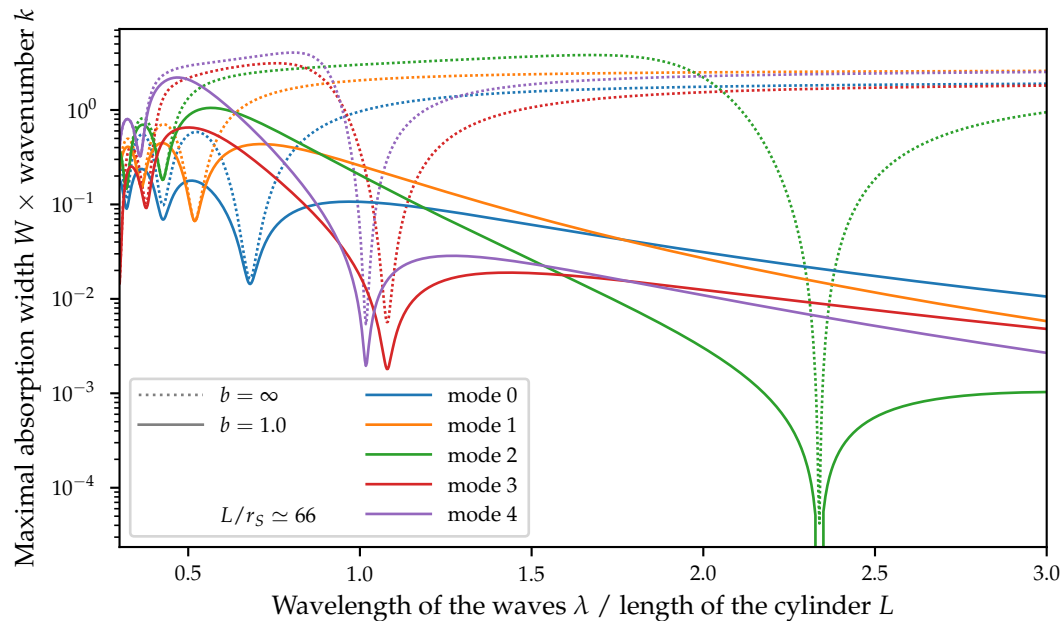

Figure 5. Dimensionless maximal absorption width as a function of the wavelength of the incoming waves. Each line corresponds to the absorption width of the different degrees of freedom of the S3 taken individually. The dotted lines are the unconstrained absorption widths. The solid lines are the absorption width under the constraint $b = 1.0$.

The range of wavelengths of the waves on which a mode is able to capture power is related to the wavelength of the oscillation of this mode: modes with a smaller wavelength capture energy from waves with a smaller wavelength. Although the unconstrained maximal absorption width predicts high absorption widths for waves with long wavelengths, they would require high values of $\hat{a}/\hat{A}$ and the constrained maximal absorption width is much lower.

Keep in mind the discussion of Section 3.3: a large value of $\hat{a}/\hat{A}$ is unrealistic for wave amplitude of around 1 m, but it makes sense for small wave amplitude. The dotted curves of Figure 5 represent the absorption width that can be achieved for small incoming waves. However, the waves that are of interest for production have an amplitude of the order of magnitude of 1 m and for these the unconstrained absorption width would require nonphysical deformations of the device.

On Figure 6, computations that are similar to that shown in Figure 5 are shown but this time for a device with several dofs. Overall, adding more dofs increases the ability of the device to capture energy. The unconstrained absorption width increases linearly with the number of dofs, similarly to what (7) predicts. However, the increase of the constrained maximal absorption width is much more moderate. The marginal gain is expected to be lower and lower for each new mode and the constrained maximal absorption width to converge as the number of modes increases, unlike the unconstrained one. In Figure 6, the constrained maximal absorption width appears to have converged for wavelengths that are higher than 1L. In the next section, the convergence for lower wavelength is observed by adding more modes.
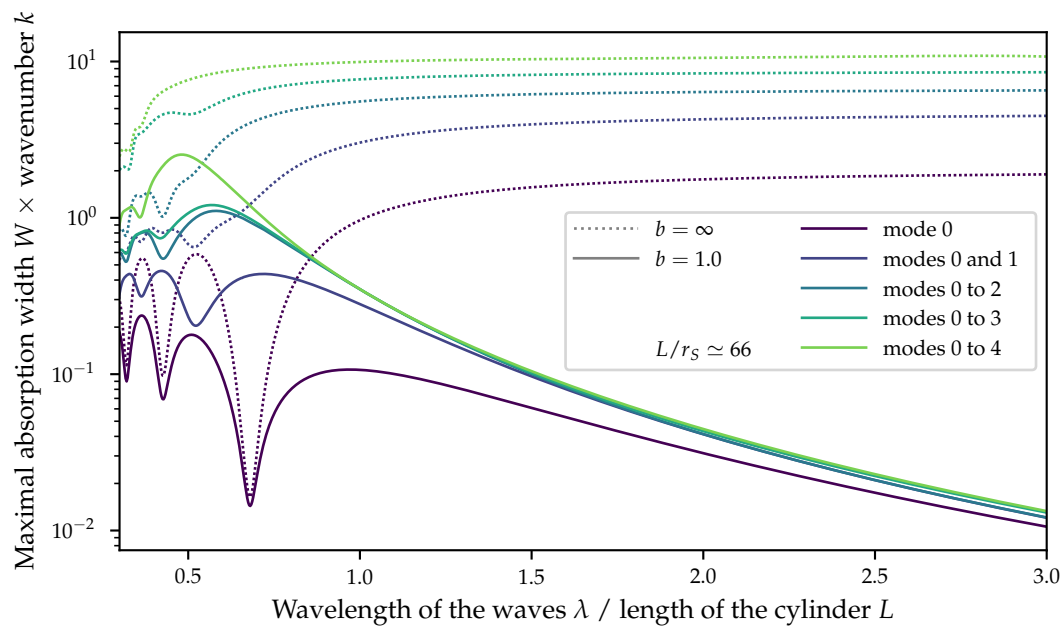
Figure 6. Dimensionless maximal absorption width as a function of the wavelength of the incoming waves. Each line corresponds to the absorption width for the combination of several modes. The dotted lines are the unconstrained absorption widths. The solid lines are the absorption widths under the constraint $b = 1.0$.

On Figure 7, a single wavelength of incoming waves is considered, but the angle of the incoming wave is varying. In the unconstrained case, (7) can now be exactly verified: the averaged absorption width over all directions is equal to the number of dofs that we model. Some dofs have a higher unconstrained maximal absorption width for waves that are not traveling in the same direction as the device. This can be explained by the schematics in Figure 8: waves that excite a given mode of deformation when traveling along the device can excite another one when traveling in a different direction. However, this theoretical effect might not be applicable in practice: this effect gets much lower when a constraint is applied on the maximal deformation. The constrained maximal absorption width of several modes appears to be almost monotonous with respect to the direction of the incoming waves.

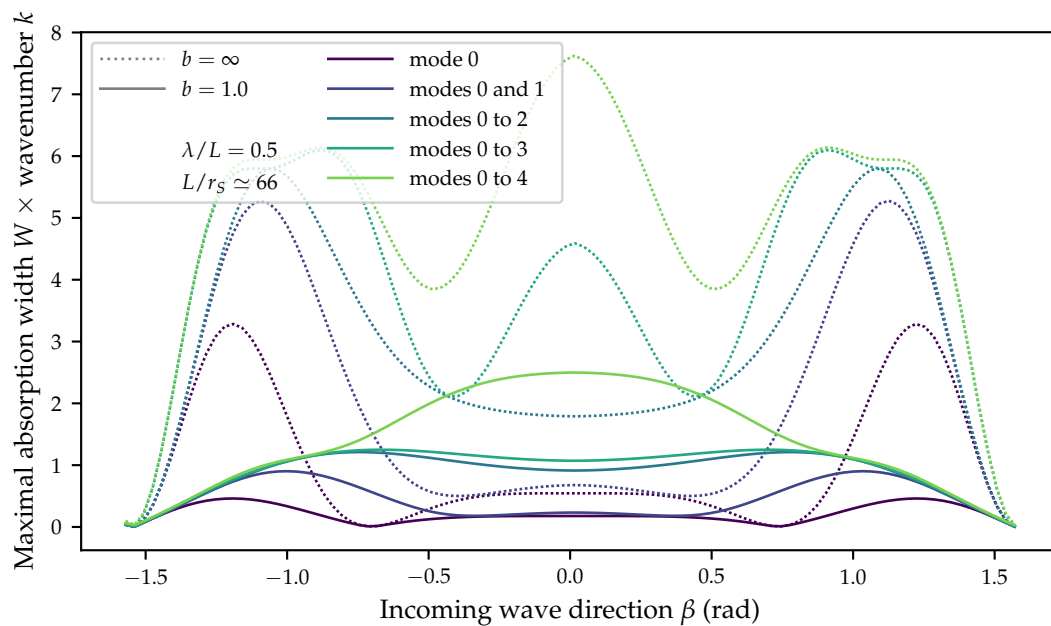Overall, the results are similar to the simplified model that is discussed in [11].

Figure 7. Dimensionless maximal absorption width as a function of the direction of the incoming waves. Each line corresponds to the absorption width for the combination of several modes. The dotted lines are the unconstrained absorption widths. The solid lines are the absorption widths under the constraint $b = 1.0$.
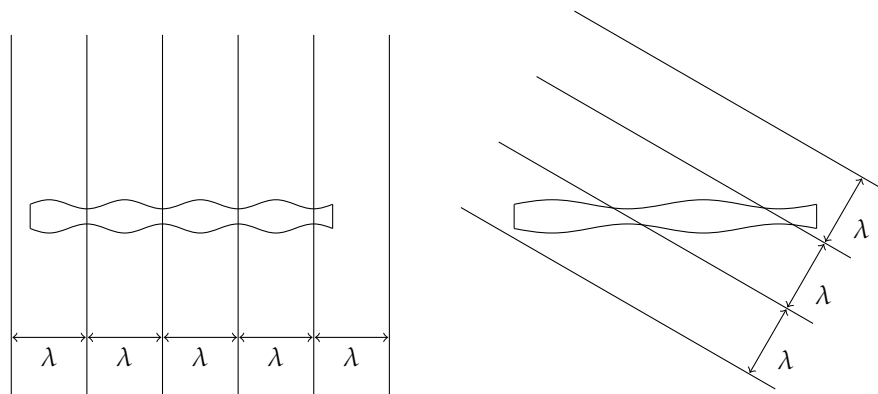

Figure 8. A wave with wavelength λ propagating in the direction of the cylinder is exciting the mode of wavelength λ. When the same wavelength is propagating with an angle β with respect to the cylinder, it can excite a mode of wavelength $\lambda / \cos(\beta)$.

3.5. Comparison with the Linear Response of the WEC

In Section 2.3, the linear model of the S3 derived in [5] has been presented. The linear equation of motion (17) can be solved to compute what would be the actual response of the WEC. In this section, the power absorbed by this linear response is compared to the maximal deformation (9). In Figure 9, the absorption width has been plotted for both methods.

The solid lines represent the constrained maximal absorption widths, similar to the solid lines presented in Figure 6, but now with more modes. The constrained maximal absorption width, which is maximal but assumes a moderate deformation of the cylinder, is of the order of magnitude of one to 10 diameters of the cylinder.

As discussed in Section 3.2, the unconstrained absorption width has not been computed for this number of modes. It can be assumed to be of the order of magnitude of 10 to 100. By definition, all of the other curves should be lower.

The dash-dotted line is the absorption width of the linear response, that is of the solution of the equation of motion (17). Unlike the maximal absorption width, the linear response depends on the dissipation coefficient η. Figure 9 represents two values of η.
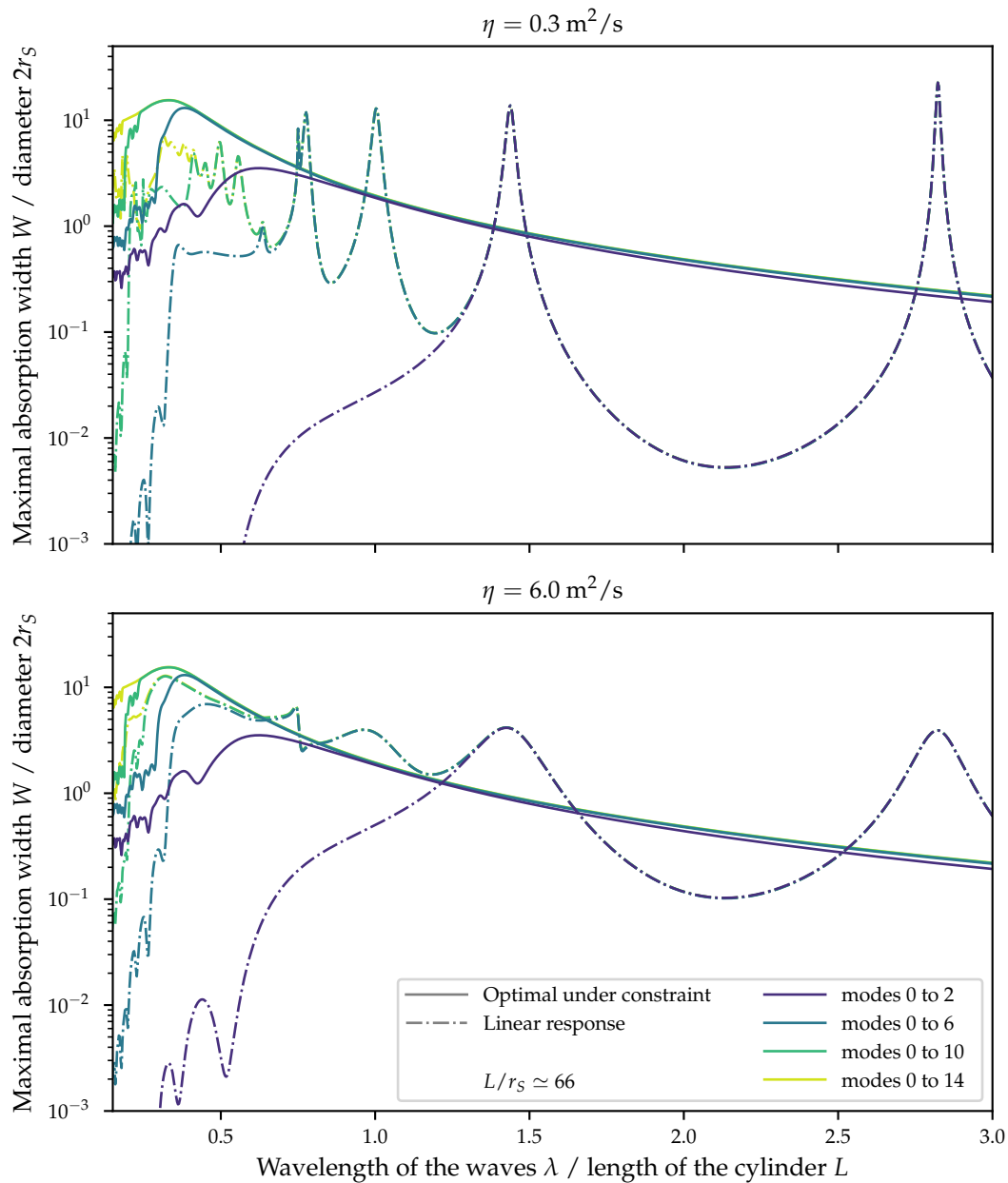

Figure 9. Dimensionless absorption width as a function of the wavelength of the incoming waves for the optimal deformation under constraint and the linear response for two values of η. The solid lines represent the constrained maximal absorption widths. The dash-dotted lines correspond to the linear response.

For all curves, adding more modes results in an increase of the predicted absorption width, until convergence is reached. The lower the wavelength, the more modes are necessary to reach convergence. Indeed, the modes of deformation of the S3 are best to capture wave energy for wavelengths near their own characteristic wavelength.

For $\eta = 0.3\,\mathrm{m}^2\,\mathrm{s}^{-1}$, the absorption width of the linear response is one or two orders of magnitude lower than the constrained maximum for most wavelengths. In practice, the excitation of the cylinder

by the incoming waves does not exactly produce the deformation that would capture the most power for this η. Some resonance peaks are visible for some wavelengths, especially near 0.75*L*, 1*L*, 1.5*L* and 2.75*L*, where *L* is the length of the cylinder. On the resonance peaks, the absorption width is high (around 10 diameters of the cylinder). The absorption width on these peaks is higher than the maximal reasonable absorption width (solid lines). It must then correspond to an amplitude of deformation that is unrealistic. The linear model only allows for us to predict that the deformation would be out of the scope of the linear model at this point.

Combining the information of the linear response (dash-dotted lines) and the maximal amplitude under constraint (solid lines) by taking the minimum of both sets of curves could be a way to have a more accurate model: when the predicted linear response is low, it is expected to be an accurate prediction; when it is high and leads to nonphysical deformations, the best deformation in the range of physical deformation might be a better guess.

In between peaks, the absorption width is very low, which can be explained by the phenomenon of anti-resonance. The two nearest modes are reacting in phase opposition and they counteract each other.

For $\eta = 6.0\,\text{m}^2\,\text{s}^{-1}$, the absorption width of the linear response is higher. This value of η has been selected as being close to the optimal value of η: for a lower value of η, the dissipation is too weak to capture any energy, whereas, for a higher value of η, the device is too stiff and it does not interact with the waves. For this value of η, the resonance and anti-resonance phenomena are mitigated and the absorption width varies more slowly with respect to the wavelength of the waves.

The value of the absorption width of the linear response for this value of η is surprisingly close to the maximal value.

4. Discussion and Conclusions

Control strategies can be used in order to improve the response of WECs to waves. The far-field maximal absorption width can be seen as an upper bound to evaluate what would be the power captured using a perfect control strategy.

In this paper, we have only used a relatively small number of modes. It will be of interest to use more modes. For that, finer meshes will be required to ensure that low-wavelength modes are correctly modeled by the BEM solver. Adding more modes can only result in a higher absorption width. The results that are presented in this paper can be seen as a lower bound of the absorption width in this respect.

Several mathematical issues related to the resolution of the optimization problem (9) remain open. The constraints that have been applied in this paper have no physical meaning when several dofs are involved. They have only been chosen because they were easy to implement with the numerical optimizer and lead to results without noise. More sophisticated numerical optimizers need to be considered to improve the relevance of this method. In the future, the research should focus on incorporating a realistic constraint for the absorption width optimization. It could for instance be based on the maximum physical radial deformation over the entire WEC length.

The method shows that the absorption width of the S3 WEC is larger for wavelengths that are smaller than the device length. In practice, it means that S3 WECs will be longer than the maximal wavelength to be captured on the targeted production site.

This far field model could be used to explore the influence of the design parameters of the S3 WEC on its absorption width. This would greatly help to refine the R & D strategy for the S3 development. It would also allow for defining the physical characteristics of a commercial S3 WEC, which is a key input to the business case.

Author Contributions: M.A. proposed the far-field maximal power absorption approach. M.D. and M.A. performed the numerical simulations. M.A. and M.D. wrote the draft article. P.J. made incisive intellectual contributions to the engineering aspects of the work. All authors participated in the analysis and interpretation of results. F.D. and P.J. oversaw and gave feedback on the drafts. All authors have read and agreed to the published version of the manuscript.

Conflicts of Interest: The authors declare no conflict of interest.

References

1. Desmars, N.; Tchoufag, J.; Younesian, D.; Alam, M.R. Interaction of surface waves with an actuated submerged flexible plate: Optimization for wave energy extraction. *J. Fluids Struct.* **2018**, *81*, 673–692. [CrossRef]

2. Tay, Z.Y.; Wei, Y. Power enhancement of pontoon-type wave energy convertor via hydroelastic response and variable power take-off system. *J. Ocean. Eng. Sci.* **2020**, *5*, 1–18. [CrossRef]

3. Mei, C.C. Nonlinear resonance in Anaconda. *J. Fluid Mech.* **2014**, *750*, 507–517. [CrossRef]

4. Renzi, E. Hydroelectromechanical modelling of a piezoelectric wave energy converter. *Proc. R. Soc. A* **2016**, *472*, 20160715. [CrossRef]

5. Babarit, A.; Singh, J.; Mélis, C.; Wattez, A.; Jean, P. A numerical model for analysing the hydroelastic response of a flexible Electro Active Wave Energy Converter. *J. Fluid Struct.* **2017**, *74*, 356–384. [CrossRef]

6. Folley, M. *Numerical Modelling of Wave Energy Converters: State-of-the-Art Techniques for Single Devices and Arrays*; Academic Press: Cambridge, MA, USA, 2016.

7. Babarit, A. *Ocean Wave Energy Conversion*; Elsevier: Amsterdam, The Netherlands, 2018.

8. Newman, J. Absorption of wave energy by elongated bodies. *Appl. Ocean Res.* **1979**, *1*, 189–196. [CrossRef]

9. Farley, F. Wave energy conversion by flexible resonant rafts. *Appl. Ocean Res.* **1982**, *4*, 57–63. [CrossRef]

10. Farley, F. Far-field theory of wave power capture by oscillating systems. *Philos. Trans. R. Soc. A Math. Phys. Eng. Sci.* **2012**, *370*, 278–287. [CrossRef] [PubMed]

11. Ancellin, M.; Babarit, A.; Jean, P.; Dias, F. Far Field Maximal Power Absorption of a Bulging Cylindrical Wave Energy Converter: Preliminary Numerical Results. Actes des Journées de l'Hydrodynamique 2018. 2018. Available online: http://website.ec-nantes.fr/actesjh/images/16JH/Articles/JH2018_papier_07D_Ancellin_et_al.pdf (accessed on 15 October 2020).

12. Dong, M. *Hydro-Elastic Response of a Bulging Cylindrical Wave Energy Converter*; Internship Report; University College Dublin: Dublin, Ireland, 2019.

13. Falnes, J.; Kurniawan, A. Fundamental formulae for wave-energy conversion. *R. Soc. Open Sci.* **2015**, *2*, 140305. [CrossRef] [PubMed]

14. Zheng, S.; Meylan, M.H.; Zhu, G.; Greaves, D.; Iglesias, G. Hydroelastic interaction between water waves and an array of circular floating porous elastic plates. *J. Fluid Mech.* **2020**, *900*. [CrossRef]

15. Ancellin, M.; Dias, F. Capytaine: A Python-based linear potential flow solver. *J. Open Source Softw.* **2019**, *4*, 1341. [CrossRef]

16. Babarit, A.; Delhommeau, G. Theoretical and numerical aspects of the open source BEM solver NEMOH. In Proceedings of the 11th European Wave and Tidal Energy Conference (EWTEC2015), Nantes, France, 6–11 September 2015.

17. Virtanen, P.; Gommers, R.; Oliphant, T.E.; Haberland, M.; Reddy, T.; Cournapeau, D.; Burovski, E.; Peterson, P.; Weckesser, W.; Bright, J.; et al. SciPy 1.0: Fundamental algorithms for scientific computing in Python. *Nat. Methods* **2020**, *17*, 261–272. [CrossRef] [PubMed]

18. Kraft, D. A software package for sequential quadratic programming. In *Forschungsbericht- Deutsche Forschungs- und Versuchsanstalt fur Luft- und Raumfahrt*; DFLVR: Oberpfaffenhofen, Germany, 1988; Volume DFLVR-FB 88-28.

19. Hunter, J.D. Matplotlib: A 2D graphics environment. *Comput. Sci. Eng.* **2007**, *9*, 90–95. [CrossRef]

20. Hoyer, S.; Hamman, J. xarray: N-D labeled arrays and datasets in Python. *J. Open Res. Softw.* **2017**, *5*. [CrossRef]

21. Lam, S.K.; Pitrou, A.; Seibert, S. Numba: A LLVM-Based Python JIT Compiler. In *Proceedings of the Second Workshop on the LLVM Compiler Infrastructure in HPC*; Association for Computing Machinery: New York, NY, USA, 2015. [CrossRef]

22. Ancellin, M.; Dias, F. Using the floating body symmetries to speed up the numerical computation of hydrodynamics coefficients with Nemoh. In Proceedings of the 37th International Conference on Ocean, Offshore and Arctic Engineering (OMAE2018), Madrid, Spain, 17–22 June 2018. [CrossRef]

Publisher's Note: MDPI stays neutral with regard to jurisdictional claims in published maps and institutional affiliations.